Draft version July 25, 2022
Typeset using LaTeX **manuscript** style in AASTeX631

Orbital Determination Report on 1994 PC1

Team 3 - Yellowstone: Blackman, A.,[1] Yang, G.,[1] and Zhao, M.[1]

[1] *Summer Science Program and Sommers-Bausch Observatory, University of Colorado Boulder, Boulder, CO, 80309, USA*

(Received July 22, 2022; Revised July 25, 2022; Accepted July 22, 2022)

ABSTRACT

Near-Earth Asteroids pose a potential danger to Earth, both on a global and local scale. By using data collected throughout June and July 2022 on the asteroid 1994 PC1, the orbital elements of the asteroid were determined, allowing for the generation of an ephemeris for 1994 PC1 in the future and the modeling of its orbit. The method used, the Method of Gauss, can be generalized to any other Near-Earth Asteroid, allowing for a fairly accurate approach towards tracking their orbits. Results show that 1994 PC1 has a semi-major axis of $1.3484AU \pm 0.0012AU$*, an eccentricity of* 0.32947 ± 0.00023*, an inclination of* $33.461^\circ \pm 0.064^\circ$*, a longitude of ascending node of* $117.873^\circ \pm 0.013^\circ$*, an argument of perihelion of* $47.467^\circ \pm 0.070^\circ$*, and a mean anomaly of* $83.81^\circ \pm 0.10^\circ$*. These values allow for the tracking of 1994 PC1's orbit, and when this process is applied to other Near-Earth Asteroids, it can allow for sufficient preparation of a potential Earth collision.*

1. INTRODUCTION

There are a myriad of different types of objects and debris that can be found in the solar system. While it is the largest of these objects such as the planets and moons that often garner the most attention, it is the much smaller pieces of debris that prove more dangerous. There are a relatively small number of large objects, and due to the large size of these objects, they are easily observable and have little chance for hidden danger. Conversely, it is the much smaller pieces of debris that pose a greater danger to Earth. Due to the sheer quantity of debris, it is unfeasible to constantly track them all, leading to the constant presence of hidden danger. This debris can be split into two main categories: comets and asteroids. Comets are fast moving objects made mostly of ice, dust, and rocky material. They can enter and exit the solar system extremely quickly. (Wall, 2014 [11]). The second category, asteroids, can be further subdivided into categories such as Near Earth Asteroids (NEAs) and Mars crossing asteroids. NEAs are celestial bodies with perihelion distance (farthest possible distance from the sun) of no more than ≈ 1.3 Astronomical Units (AU). Mars crossing asteroids are further outwards in the solar system so the orbits cross the orbit of Mars. There are also other types of asteroids such as Trojan asteroids, which are at the stable Lagrange points (L4,L5) of a planet. However, the NEAs pose the greatest risk towards colliding with Earth. While the overall risk of collision with a NEA is small, a potential collision could occur at any time and may be catastrophic (Garshnek et al., 2000 [3]). It only takes an asteroid with a diameter of 25 meters to one kilometer to cause local damage, and an asteroid with a diameter of one kilometer or more to have global effects (NASA, 2017 [8]).

Despite the active danger that NEAs pose, only a small portion of the asteroids have been tracked (Figure 1). While sky surveys constantly add to the list of NEAs, there is still a large gap for NEAs with a diameter of 1km and less (Harris, Chodas, 2015 [4]). However, an asteroid of this size is dangerous enough to cause local damage (NASA, 2017 [8]).

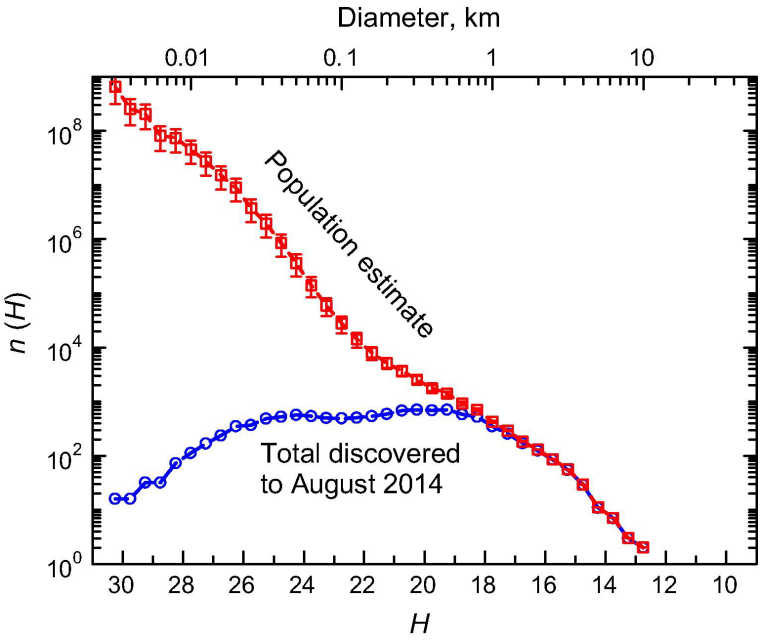

Figure 1. Population of Near Earth Asteroids (Adapted from Harris et al. 2015 [4])

The most prominent search campaigns for NEAs are the Space Guard Survey and the The Large Synoptic Survey Telescope (LSST). The Space Guard Survey (1998 - 2010) tracked most of the NEAs with an diameter of over one kilometer. The LSST project, commenced in 2008, is estimated to be completed in 2030 and expects to track 61% of the near Earth objects brighter than H=22 (Jones et al., 2017 [7]). Comparing H=22 to Figure 1, this region covers asteroids with an diameter of 100 meters and larger. However, this still leaves out many potentially dangerous asteroids.

With this lack of data, it is imperative that NEA orbits be determined and tracked to ensure preparation for potential Earth impacts. This paper outlines the use of the Method of Gauss to track asteroid 1994 PC1 over three sets of observations. While this paper focuses solely on one asteroid, the method described can be applied to any NEA. 1994 PC1 is an Apollo asteroid, meaning it has a perihelion interior to Earth's aphelion. This asteroid is of particular interest due to its close flybys with the Earth. Most recently, 1994 PC1 was 0.0129 AU away from Earth at 21:51 UTC on January 18, 2022 (Irizarry, 2022 [6]).

To determine an asteroid's orbit, the six orbital elements must be calculated: the semimajor axis (a), eccentricity (e), inclination (i), longitude of the ascending node (Ω), argument of perihelion (ω), and mean anomaly (M) (Figure 2). The semimajor axis (α) is the distance of half the major axis of the elliptical orbit with Sun is at a focus. The semimajor axis is used as a measure of the size of the elliptical orbit, and it is typically found in astronomical units. The eccentricity (e) is a measurement of the elongation of the ellipse. The eccentricity is a value from zero to one, where an orbit with an eccentricity of zero is circular, and one with an eccentricity of one is hyperbolic. The inclination (i) of the asteroid is the angle between the orbital plane of the asteroid and the orbital plane of the Earth (the ecliptic plane). The longitude of the ascending node (Ω) is the angle between the ascending node (the point at which the asteroid starts moving from south to north on the ecliptic plane) and the vernal equinox. The argument of the perihelion(ω) is the angle between the vernal equinox and the perihelion. The mean anomaly (M) is the angular position that the asteroid would occupy if it had a true circular orbit, using the center of the ellipse as the reference point to measure degrees from the perihelion point.

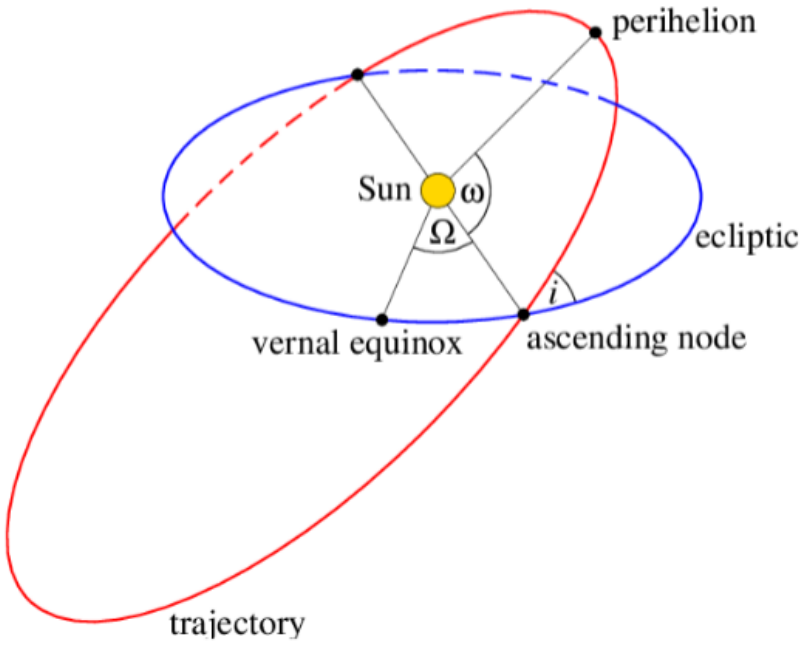

Figure 2. Visualization of Orbital Elements (Adapted from Domingue, 2022 [2])

For this paper, the Method of Gauss was used to determine the orbital elements. The Method of Gauss relies on having three total observations of the NEA, roughly evenly spaced out in time. The Method of Gauss was used rather than Laplace's method because it is more accurate for quickly moving asteroids, while Laplace's method works better for Main Belt asteroids. For each of the three observations, a set of right ascension (RA) and declination (Dec) values was obtained. For the purposes of this paper, four observations of 1994 PC1 were done to test accuracy of the final values.

2. OBSERVATIONS AND IMAGE PROCESSING

2.1. *Data Acquisition*

The position data for the asteroid was collected at the Sommers-Bausch Observatory (SBO) (observatory code 463) at the University of Colorado Boulder in Boulder, Colorado, United States of America. The observatory is at a latitude of $+40^\circ\ 00'\ 13.36''$ N, a longitude of $-105^\circ\ 15'\ 467.84''$ W, and an altitude of 1653 meters (University of Colorado, n.d. [10]). The observatory's Artemis (East) telescope was used, a CDK20 Optical Tube Assembly PlaneWave Instruments telescope (Figure 3). The telescope has a 20-inch (0.508 meter) aperture, a 3454mm focal length, a f/6.8 focal ratio, and a 52 x 52 arcminute field (PlaneWave Instruments, n.d. [9]). Images were taken with a SBIG Imaging Systems STF-8300 camera (Figure 4), which uses a Kodak KAF-8300 CCD. The CCD is 17.96 x 13.52mm with a 3326 x 2504 pixel array, and a total pixel count of 8.3 million. The CCD has a gain of $0.37\text{e}^-/\text{ADU}$ and a full well capacity of $\backsim 25,500e^-$ (Diffraction Limited/SBIG, n.d. [1]).

Figure 3. CDK20 Optical Tube Assembly PlaneWave Instruments telescope (PlaneWave Instruments, n.d. [9])

Figure 4. SBIG Imaging Systems STF-8300 camera (Diffraction Limited/SBIG, n.d. [1])

When collecting data with this equipment, a specific process was followed for each observation session. Prior to each session, an ephemeris for asteroid 1994 PC1 was generated with JPL Horizons. The ephemeris contained the approximate RA, Dec, altitude, azimuth, and magnitude of 1994 PC1 at fifteen minute intervals from 05:00-08:00 UTC. The RA and Dec for 06:00 UTC, the beginning of the planned observation session, was used in SAOImage DS9 to generate a star chart picturing the area of the sky surrounding asteroid 1994 PC1.

While observing, TheSkyX software was used to control the telescope. For each observation session, prior teams had already focused the telescope. TheSkyX was used to slew the telescope to the correct RA and Dec of 1994 PC1 for the current time, and a test image was taken. If the star field imaged matched the field of the star chart, the data collection images were taken. Each observation session had three light series of three images each. The series were taken ten minutes apart, and each image had a 40 second exposure and was taken with a UV/IR Cut filter. In addition, dark and flat frames were taken for future data reduction. Dark frames are frames that were taken with the lens cap on the camera. These frames adjust for the random electronic thermal noise from the camera sensor. Flat frames are frames taken of a simple white sheet illuminated by a LED light. These frames are used to adjust for the gradients and dust that may be present on the telescope itself. During observations, a total of five dark and five flat frames were taken, each with an exposure time of 40 seconds which matches the exposure time used for the the light frames taken of 1994 PC1.

If necessary, additional series were taken during an observation session if some were not usable. This happened in instances when poor weather conditions impacted the images. There were ultimately four successful observation sessions, defined as sessions where there were a sufficient number of series and images with clear weather (Table 1).

Table 1. Successful observations of 1994 PC1

Observation Date	Time of Image (UTC)	Observatory	Filter	Exposure Time (seconds)	Notes
June 28th, 2022	06:21:39.157	SBO (463)	UV/IR Cut	40	some cloud coverage
June 28th, 2022	06:32:12.727	SBO (463)	UV/IR Cut	40	clear sky
June 28th, 2022	06:41:51.849	SBO (463)	UV/IR Cut	40	clear sky
July 9th, 2022	06:15:40.179	SBO (463)	UV/IR Cut	40	clear sky
July 9th, 2022	06:25:57.975	SBO (463)	UV/IR Cut	40	clear sky
July 9th, 2022	06:35:51.384	SBO (463)	UV/IR Cut	40	clear sky
July 10th, 2022	06:35:52.073	SBO (463)	UV/IR Cut	40	clear sky
July 10th, 2022	06:45:57.148	SBO (463)	UV/IR Cut	40	clear sky
July 10th, 2022	06:55:52.213	SBO (463)	UV/IR Cut	40	asteroid near star
July 12th, 2022	06:21:46.864	SBO (463)	UV/IR Cut	40	clear sky
July 12th, 2022	06:30:58.409	SBO (463)	UV/IR Cut	40	clear sky
July 12th, 2022	06:41:09.864	SBO (463)	UV/IR Cut	40	clear sky

2.2. *Astrometry and Photometry*

After each observation, all the images were processed using astrometry and photometry. The process of astrometry was used to obtain the RA and Dec values for the asteroid while the process of photometry was used to obtain the magnitude values of the asteroid. First, the raw images from each observation period were corrected for flat and dark frames. Al flat and dark frames were stacked with the other frames of the same time to create a master flat frame and a master dark frame (Figure 5).

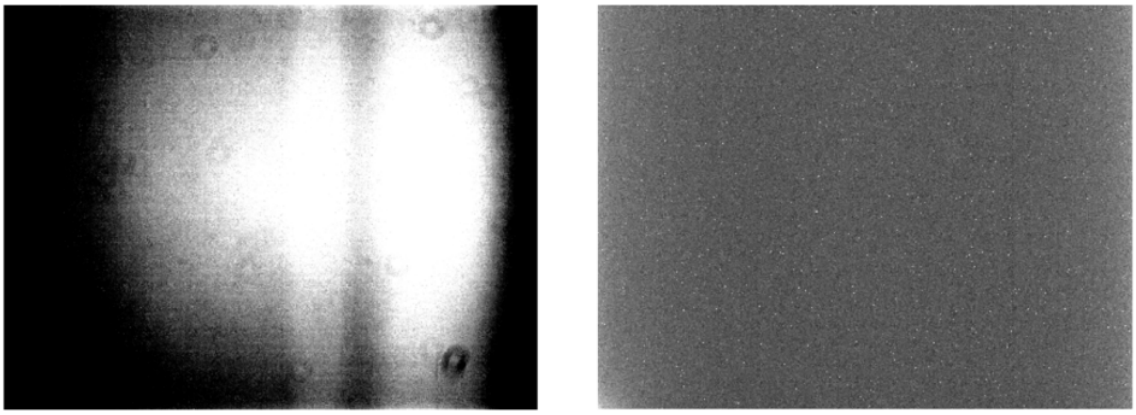

Figure 5. *Master Flat (left) and Master Dark (right) Frames from June 28th, 2022*

These master flat and dark frames were recreated for each observation session as there was nightly variance in the flat and dark frames. After obtaining the master flat and dark frames, they are applied to the raw images from the light series. The dark and flat corrected light frames were then stabilized using AstroImageJ's image stabilizer with the settings at a translation transformation, a template update coefficient 0.90, a maximum iteration number of 200, and an error tolerance of 0.0000001. It should be noted that the images had minimal changes after undergoing the image stabilizer process due to the short exposure times and how the was telescope tracking the star field.

At this point, astrometry was used to determine the RA and Dec values of 1994 PC1. The LSPR method was used to determine the position of the asteroid by comparing it to nearby stars in the field. To undergo this process, the images were uploaded to Astrometry.net, which gave the RA and

Dec. Apertures were used on AstroImageJ to find the RA and Dec of 1994 PC1 for each observation session (Table 2). The middle series from each observation was chosen to undergo astrometry to ensure consistency.

Table 2. RA and Dec of 1994 PC1

Observation Date	RA (hours)	Dec (degrees)
June 28th, 2022	19.71	11.29
July 9th, 2022	19.24	-0.34
July 10th, 2022	19.11	-3.61
July 12th, 2022	19.20	-1.44

Next, to determine the visual magnitude (V_{mag}) values, photometry was done. Photometry was done on only one of the images of each series, as the 40 second gap between images within a series was unlikely to create any noticeable difference in the V_{mag} value of 1994 PC1. As such, the middle image from each series was chosen for consistency with the images used for astrometry. Similar to astrometry, photometry used the Astrometry.net files with the RA and Dec. Using the aperture setting on AstroImageJ, a series of three apertures was made (Figure 6). The object aperture was changed so that it only contained the object of interest. The inner annulus was a dead zone region where the pixels were a transition from the object of interest to the background. As such, this region was not used by AstroImageJ in the final calculation of the Source-Sky values. However, it was still essential to ensure accuracy in the pixel values of the asteroid and sky. The outer annulus was used to measure the background pixel count. It was set as large as possible without infringing onto another star, which would disrupt the background pixel count (Figure 6). From these apertures, the value of Source-Sky was obtained from AstroImageJ. The software measured the pixel count of the source

(the object aperture) and the pixel count of the outer annulus. Subtracting the two values yielded the value for Source-Sky of the object of interest.

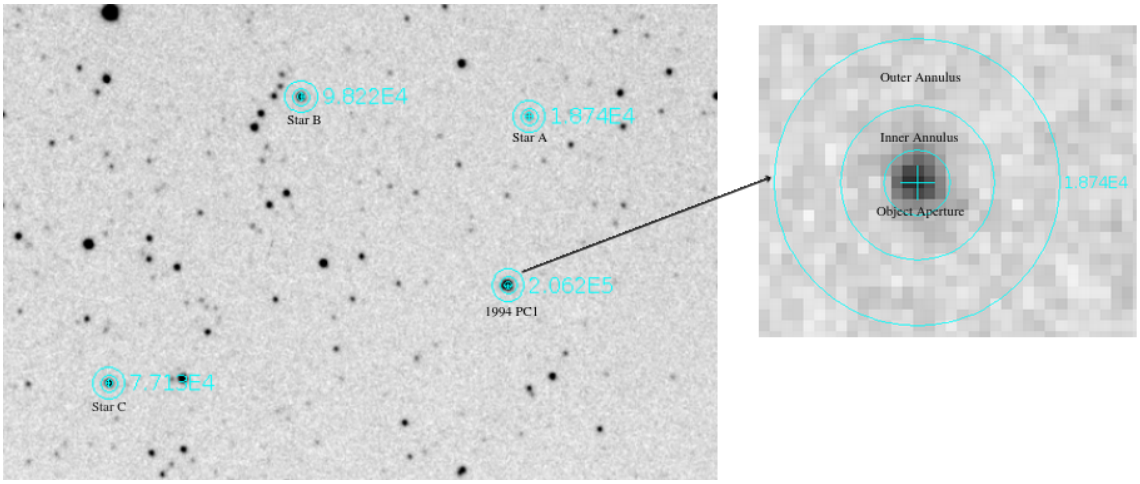

Figure 6. *Photometry Apertures for Series 1 of July 12th, 2022*

The end goal of photometry was to obtain a value for the V_{mag} of 1994 PC1. To do so, a comparison had to be made between the object of interest (1994 PC1) and other objects of known magnitude. To ensure the comparison was accurate, three stars were chosen as comparisons. The chosen stars had a fairly low V_{mag}, without the pixel count of the image crossing the saturation point. This allowed for the largest Source-Sky values, leading to a smaller percentage error present in the data points. Then, to determine the V_{mag} of 1994 PC1, the Source-Sky of three stars was determined as well as their established V_{mag} values. The V_{mag} values of the stars were obtained from SAOImage Ds9 with the II/336 - AAVSO Photometric All Sky Survey database (Henden et al., 2016 [5]). By matching the selected stars in the database with the image on SAOImage Ds9, the magnitudes of the target stars were established. The following formula was used to relate the Source-Sky to the V_{mag} of the asteroid (Equation 1).

$$\log_{10}\left(\frac{F_1}{F_2}\right) = \log_{10}(2.5^{m_2-m_1}) \tag{1}$$

By applying relevant variable names, the following equation was established (Equation 2).

$$V_{\text{asteroid}} = -2.5 \log_{10} \left((\text{Source} - \text{Sky})_{\text{asteroid}} \right) + B \tag{2}$$

All values are known in equation 2 except for B. However, B is simply the $-2.5 \log_{10} \left((\text{Source} - \text{Sky})_{\text{stars}} \right)$. As three stars were chosen rather than just one, there were three different values of Source-Sky. To address this, a line of best fit was created using a least squares regression line. When generating this line of best fit, the slope was around -2.5, and the y-intercept was the value of B. After generating the values of B for each series, equation 2 was used to calculate the experimental value of V_{mag} for 1994 PC1. These values were compared to the approximate V_{mag} obtained from JPL Horizons (Table 3).

Table 3. V_{mag} *of* 1994 *PC*1 *through* 3 *Observations*

Observation Date	Time of Image (UTC)	Experimental V_{mag}	JPL V_{mag}	Percentage Difference
June 28th, 2022	06:21:39.157	17.52	16.78	1.08%
June 28th, 2022	06:32:12.727	17.98	16.78	6.90%
June 28th, 2022	06:41:51.849	17.90	16.78	6.46%
July 9th, 2022	06:15:40.179	16.26	16.48	0.34%
July 9th, 2022	06:25:57.975	16.28	16.48	1.34%
July 9th, 2022	06:35:51.384	16.38	16.48	1.08%
July 10th, 2022	06:35:52.073	16.60	16.47	0.79%
July 10th, 2022	06:45:57.148	16.96	16.47	2.93%
July 10th, 2022	06:55:52.213	16.50	16.47	0.18%
July 12th, 2022	06:21:46.864	16.72	16.46	1.57%
July 12th, 2022	06:30:58.409	16.97	16.46	3.05%
July 12th, 2022	06:41:09.864	16.89	16.46	2.58%

2.3. *Determination of Errors in Astrometry*

To determine the error on the calculated RA and Dec values, Nova Astrometry was used. The software of the website uses the Least Plate Square Reduction to calculate the differences in positions between stars in the predicted star field and the stars in the light frame taken. Through comparing the two, a corr.fits file was produced that was used to determine errors in the observed RAs and Decs. This then is used in the Monte Carlo simulations to determine the error in the orbital elements. Table 3 only features the RA and Dec of the middle series of each observing night due to the minimal change of position in the asteroid throughout the 30 minute periods.

2.4. *Results*

The RA and Dec was determined with the appropriate errors for each observation session (Table 3).

Table 3. RA and Dec Values of 1994 PC1 with Errors

Julian Date	RA	Dec
2459758.77236952	19hr 42min 49.18s ($\pm 0.02s$)	$11°16'41.6''(\pm 0.2'')$
2459769.76803211	19hr 14min 23.34s ($\pm 0.01s$)	$-00°20'05.9''(\pm 0.2'')$
2459772.77150936	06hr 41min 51.85s ($\pm 0.01s$)	$-03°36'46.3''(\pm 0.1'')$

3. ORBIT DETERMINATION

3.1. *Methods*

The Method of Gauss was used to determine the orbit of 1994 PC1. The middle observations from the observation sessions on June 28th, 2022, July 9th, 2022, and July 12th, 2O22 were used to determine the orbital elements. The observation from July 10th, 2022 was not used as only three observations were needed. This was excluded because the asteroid crossed near a set of three bright stars which made it impossible to exclude the stars in the aperture regions. Thus, the accuracy of the RA and Dec could be negatively affected.

Before starting the Method of Gauss, some units, constants, and variables must be defined. The units of AUs and Gaussian days were chosen to allow $\mu = GM = 1$. Other needed constants can also be converted to Gaussian days and AUs: $k = 0.01720209894$ Gaussian days per Julian day, and the speed of light (c) = 173.144632674 AU per Julian day. Let r_i, R_i, and ρ_i be the sun to asteroid position vector, the Earth to sun position vector, and the Earth to asteroid position vector respectively during the ith observation.

Values for r_2 were estimated to serve as the staring values for the Method of Gauss. To determine r_2, the scalar equation of Lagrange was used. To start the scalar equation of Lagrange, several constants needed to be set. The RA and Dec values obtained from the observations were converted to $\hat{\rho}$ (Equation 3).

$$\hat{\rho} = (\cos\alpha\cos\delta)\hat{i} + (\sin\alpha\cos\delta)\hat{j} + (\sin\delta)\hat{k} \tag{3}$$

Next, the starting τ values were determined from the times of observation (equation 4-6). The D constants used in both the Lagrange scalars equation and the Method of Gauss loop (Equation 7-11).

$$\tau = k(t_3 - t_1) \tag{4}$$

$$\tau_3 = k(t_3 - t_2) \tag{5}$$

$$\tau_1 = k(t_1 - t_2) \tag{6}$$

$$D_o = \hat{\rho}_1 \cdot (\hat{\rho}_2 \times \hat{\rho}_3) \tag{7}$$

$$D_{1j} = (\overrightarrow{R_j} \times \hat{\rho}_2) \cdot \hat{\rho}_3 \tag{8}$$

$$D_{2j} = (\hat{\rho}_1 \times \overrightarrow{R_j}) \cdot \hat{\rho}_3 \tag{9}$$

$$D_{3j} = \hat{\rho}_1 \cdot (\hat{\rho}_2 \times \overrightarrow{R_j}) \tag{10}$$

$$\text{where } j = 1, 2, 3 \tag{11}$$

Having the general constants, other constants required for the scalar equation of Lagrange were defined (Equation 12 - 21).

$$u_2 = \frac{\mu}{r_2^3} \tag{12}$$

$$A_1 = \frac{\tau_3}{\tau} \tag{13}$$

$$B_1 = \frac{A_1}{6}(\tau^2 - \tau_3^2) \tag{14}$$

$$A_3 = -\frac{\tau_1}{\tau} \tag{15}$$

$$B_3 = \frac{A_3}{6}(\tau^2 - \tau_1^2) \tag{16}$$

$$A = \frac{A_1 D_{21} - D_{22} + A_3 D_{23}}{-D_o} \tag{17}$$

$$B = \frac{B_1 D_{21} + B_3 D_{23}}{-D_o} \tag{18}$$

$$a = -(A^2 + AE + F) \tag{19}$$

$$b = -\mu(2AB + BE) \tag{20}$$

$$c = -\mu^2 B^2 \tag{21}$$

Having all the constants, the scalar equation of Lagrange was used (Equation 22).

$$r_2^8 + ar_2^6 + br_2^3 + c = 0 \tag{22}$$

There were several roots obtained from the equation, however, some of the roots were non-real or negative. After removing those non-logical roots, there were several valid roots. Typically, all the valid roots converge on the same value. If one of the roots did not converge in the Method of Gauss, another root was used instead.

Now, the Method of Gauss was used on the appropriate guess for r_2. The first step of the Method of Gauss was the calculation of f and g (Equation 23-24).

$$f_i = 1 - \frac{\mu}{2r_2^3}\tau_i^2 \tag{23}$$

$$g_i = \tau_i - \frac{\mu}{6r_2^3}\tau_i^3 \tag{24}$$

It should be noted that the f and g values are infinite Taylor series. However, for the initial calculations of f and g, only the second series of the Taylor Series was used, as any further terms would have required knowledge of $\dot{\vec{r_2}}$. From the calculation of f_1, f_3, g_1, and g_3, several constant terms can be defined (Equation 25-29).

$$c_1 = \frac{g_3}{f_1 g_3 - g_1 f_3} \tag{25}$$

$$c_2 = 1 \tag{26}$$

$$c_3 = \frac{-g_1}{f_1 g_3 - g_1 f_3} \tag{27}$$

$$d_1 = \frac{-f_3}{f_1 g_3 - g_1 f_3} \tag{28}$$

$$d_3 = \frac{f_1}{f_1 g_3 - g_1 f_3} \tag{29}$$

With these values, ρ_1, ρ_2, and ρ_3 were calculated (Equation 30-32).

$$\rho_1 = \frac{c_1 D_{11} + c_2 D_{12} + c_3 D_{13}}{c_1 D_o} \tag{30}$$

$$\rho_2 = \frac{c_1 D_{21} + c_2 D_{22} + c_3 D_{23}}{c_2 D_o} \tag{31}$$

$$\rho_3 = \frac{c_1 D_{31} + c_2 D_{32} + c_3 D_{33}}{c_3 D_o} \tag{32}$$

Next, $\overrightarrow{r_1}$, $\overrightarrow{r_2}$, and $\overrightarrow{r_3}$ were calculated using the ρ values (Equation 33-35).

$$\overrightarrow{r_1} = \rho_1 \hat{\rho_1} - \overrightarrow{R_1} \tag{33}$$

$$\overrightarrow{r_2} = \rho_2 \hat{\rho_2} - \overrightarrow{R_2} \tag{34}$$

$$\overrightarrow{r_3} = \rho_3 \hat{\rho_3} - \overrightarrow{R_3} \tag{35}$$

With the r vectors, $\dot{\overrightarrow{r_2}}$ was found (Equation 36).

$$\dot{\overrightarrow{r_2}} = d_1 \overrightarrow{r_1} + d_3 \overrightarrow{r_3} \tag{36}$$

With $\dot{\overrightarrow{r_2}}$, all the elements necessary to calculate the final orbital elements were present. However, while all the required values were known, they were not accurate, as the Method of Gauss relies on repeating the cycle multiple times. Thus, the values of $\dot{\overrightarrow{r_2}}$, r_1, r_2, and r_3, were used to recalculate the f and g values with more terms of the Taylor series. A fourth order Taylor Series was used to calculate f and g in subsequent iterations, as further orders have a negligibly small impact on the final result. After recalculating f and g, the series of constant values were recalculated and used to redetermine better, more accurate values for $\dot{\overrightarrow{r_2}}$, r_1, r_2, and r_3. However, before the cycle was repeated, the time values used to calculate τ were corrected to account for the travel time of light (Equation 37).

$$t_i = t_{o,i} - \frac{\rho_i}{c} \tag{37}$$

Here, $t_{o,i}$ is the original times of observation and c is the speed of light. After correcting the time values, the Method of Gauss was repeated. Cycles of Method of Gauss were repeated until there was

very little to no change in the values of $\dot{\overrightarrow{r_2}}$, r_1, r_2, and r_3. After enough iterations, the values of $\overrightarrow{r_2}$ and $\dot{\overrightarrow{r_2}}$ stoped changing significantly. These values were used to determine the orbital elements of 1994 PC1. These vectors can be converted from equatorial to ecliptical coordinates by rotating them by negative tilt of the earth ε.

A python function was written to determine the orbital elements from a given $\vec{r}$, $\dot{\vec{r}}$.

First, the angular momentum vector was found (Equation 38).

$$\vec{h} = \vec{r} \times \dot{\vec{r}} \tag{38}$$

Next, the length of the semi-major axis was calculated (Equation 39).

$$a = \left(\frac{2}{|\vec{r}|} - \frac{\dot{\vec{r}} \cdot \dot{\vec{r}}}{\mu} \right)^{-1} \tag{39}$$

The eccentricity was calculated (Equation 40).

$$e = \sqrt{1 - \frac{|\vec{h}|^2}{\mu a}} \tag{40}$$

The inclination was calculated (Equation 41).

$$i = \cos^{-1} \left(\frac{h_z}{|\vec{h}|} \right) \tag{41}$$

Given the sine and cosine of an angle, the correct quadrant of the angle was found.

Using this, the longitude of ascending node was found (Equation 42-43).

$$\sin \Omega = \frac{h_x}{|\vec{h}| \sin i} \tag{42}$$

$$\cos \Omega = -\frac{h_y}{|\vec{h}| \sin i} \tag{43}$$

The angular distance from the ascending node to the asteroid was calculated (Equation 44-45).

$$\sin U = \frac{r_z}{|\vec{r}| \sin i} \tag{44}$$

$$\cos U = \frac{r_x \cos \Omega + r_y \sin \Omega}{|\vec{r}|} \tag{45}$$

The true anomaly was found (Equation 46-47).

$$\sin\nu = \frac{1}{e}\frac{a(1-e^2)}{|\vec{h}|}\frac{\vec{r}\cdot\dot{\vec{r}}}{|\vec{r}|} \tag{46}$$

$$\cos\nu = \frac{1}{e}\left(\frac{a(1-e^2)}{|\vec{r}|} - 1\right) \tag{47}$$

Using these previous steps, the argument of perihelion was calculated (Equation 48).

$$\omega = U - \nu. \tag{48}$$

The eccentric anomaly was found (Equation 49).

$$\cos E = \frac{1}{e}\left(1 - \frac{|\vec{r}|}{a}\right) \tag{49}$$

Lastly, the mean anomaly at the observation time was calculated (Equation 50).

$$M = E - e\sin E \tag{50}$$

The whole process from the RA and Dec values from observation to the calculation of the orbital elements is summarized below (Figure 7).

To determine the errors in the orbital elements, Monte Carlo simulations were used. Astrometry.net was used to do plate solutions on the reduced images. This resulted in a corr.fits file for each of the images, which contained a table on the correspondences between image and reference stars. From this, there was a list of residuals between the RA and Dec of stars in the images and the known RA and Dec of the reference stars. By finding the root mean squared average of these RA and Dec residuals, the standard deviation error was found for the asteroid RAs and Decs.

First, $N = 5000$ trials were done to estimate the error in the orbital elements. For each trial, the normal distribution was used to pick the RAs and Decs of 1994 PC1 for each observation. Then, the orbital elements were determined using these new RAs and Decs.

Figure 7. Flow Chart of the Method of Gauss

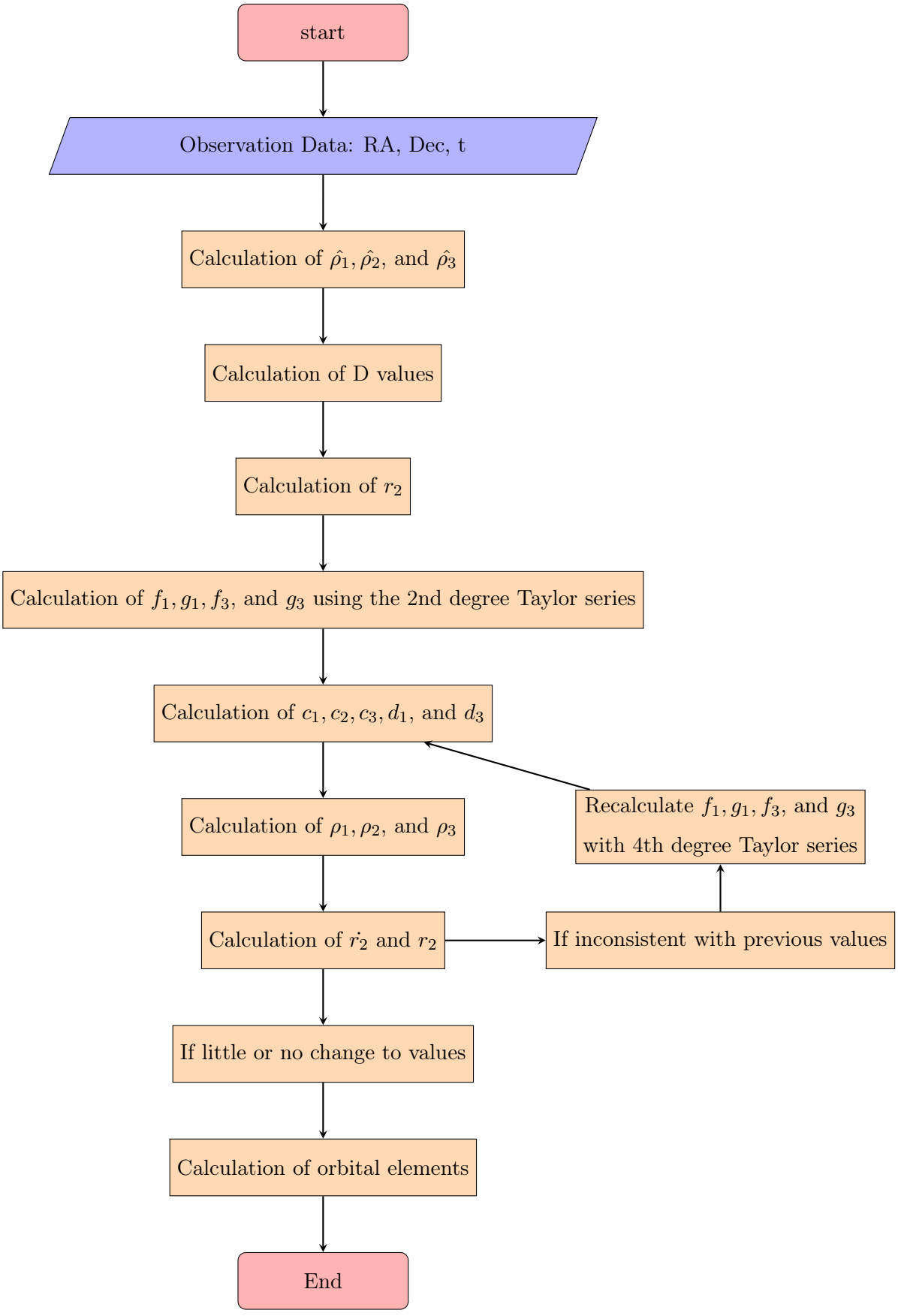

To find the error of each of orbital elements, the standard deviation of each trial's elements was found. Histograms were created for each of the orbital elements to ensure they were normally distributed.

Next, to verify if the data was consistent with itself, the ephemeris generation program was used. This is a function that returned the RA and Dec of 1994 PC1 at a specified time t given the orbital elements, a, e, T, i, Ω, and ω. First, the mean anomaly of 1994 PC1 is found at the specified time t (Equation 51).

$$M = k\sqrt{\frac{\mu}{a^3}}(t - T) \tag{51}$$

Then, the Newton-Raphson method was used to find the value of the eccentric anomaly E to satisfy a function (Equation 52).

$$f(E) = E - e\sin E - M = 0 \tag{52}$$

First, the derivative of $f(E)$ must be calculated (Equation 53).

$$f'(E) = 1 - e\cos E \tag{53}$$

This equation is used repeatedly with the previous guess for E to get a better guess for E. If x_i is the ith guess and $x_1 = M$ (Equation 54).

$$[x_{i+1} = x_i - \frac{f(x_i)}{f'(x_i)}.] \tag{54}$$

By iterating multiple times, there is a convergence upon the value of E such that $M = E - e\sin E$. The coordinates of 1994 PC1 in orbital coordinates with the positive x-axis coinciding with the perihelion is found in cartesian coordinates (Equation 55).

$$r_{\text{cart}} = \begin{bmatrix} a\cos E - ae \\ a\sqrt{1-e^2}\sin E \\ 0 \end{bmatrix} \tag{55}$$

Now, this vector is rotated multiple times to get the position of 1994 PC1 in ecliptic coordinates. First, the vector is rotated by ω around the z axis, then by i around the x axis, and lastly by Ω around the z axis. This was done through a series of matrix multiplications (Equation 56).

$$r_{\text{ecl}} = \begin{bmatrix} \cos\Omega & -\sin\Omega & 0 \\ \sin\Omega & \cos\Omega & 0 \\ 0 & 0 & 1 \end{bmatrix} \begin{bmatrix} 1 & 0 & 0 \\ 0 & \cos i & -\sin i \\ 0 & \sin i & \cos i \end{bmatrix} \begin{bmatrix} \cos\omega & -\sin\omega & 0 \\ \sin\omega & \cos\omega & 0 \\ 0 & 0 & 1 \end{bmatrix} r_{\text{cart}} \tag{56}$$

Now, this position was converted to equatorial coordinates by rotating by the tilt of the earth ε. (Equation 57).

$$r_{\text{eq}} = \begin{bmatrix} 1 & 0 & 0 \\ 0 & \cos\varepsilon & -\sin\varepsilon \\ 0 & \sin\varepsilon & \cos\varepsilon \end{bmatrix} r_{\text{ecl}}. \tag{57}$$

The range vector was then be calculated (Equation 58).

$$\vec{\rho} = \vec{r} + \vec{R}. \tag{58}$$

$\hat{\rho}$ was calculated (Equation 59).

$$\hat{\rho} = \frac{\vec{\rho}}{\rho} \tag{59}$$

Lastly, the RA(α) and Dec(δ) of 1994 PC1 was determined at the specified time t (Equation 60-62).

$$\sin\delta = \hat{\rho}_z \tag{60}$$

$$\sin\alpha = \frac{\hat{\rho}_y}{\cos\sigma} \tag{61}$$

$$\cos\alpha = \frac{\hat{\rho}_x}{\cos\sigma} \tag{62}$$

This ephemeris generator was used to find the predicted RA and Dec at the time of the third observation using the orbital elements generated from the first, second, and fourth observation. Using Monte-Carlo simulations that varied the observed RA and Dec, a predicted RA and Dec is obtained at the third observation time July 10th, 2022 06:45:57.148 UTC of

$$\text{RA: } 19:11:48.55(1),\ \text{Dec: } -01:26:43.1(1)$$

According to observations, there is an observed an RA and Dec of

$$\text{RA: } 19:11:48.55,\ \text{Dec: } -01:26:42.8$$

The predicted values for the RA and Dec are very close to the observed values, passing the self-consistency check.

3.2. *Results*

In the end, all orbital elements for 1994 PC1 were determined. When compared with JPL Horizons, the values calculated were similar with identical values up to three significant figures. JPL values were compared with the calculated value (Table 4).

Table 4. Calculated and JPL Orbital Elements for 1994 PC1

Orbital Element	JPL value	Experimental Value	Percentage Difference	z score
Semi-major Axis	1.3463AU	1.3484AU±0.0012AU	0.16%	1.88
Eccentricity	0.32836	0.32947±0.00023	0.34%	4.92
Inclination	33.488°	33.461°±0.064°	0.08%	0.42
Longitude of Ascending Node	117.899°	117.873°±0.013°	0.02%	1.98
Argument of Perihelion	47.609°	47.467°±0.070°	0.30%	2.03
Mean Anomaly	83.79°	83.81°±0.10°	0.02%	0.17

For each of the orbital elements, a Monte Carlo simulation was run with a normal distribution. It used a list of residuals between the RA and DEC of stars in the image obtained from the corr.fits files from Astrometry.net. By repeating the number of trials with regard to a normal distribution and uncertainties of RA and Dec, a series of histograms was created (Figure 8-13).

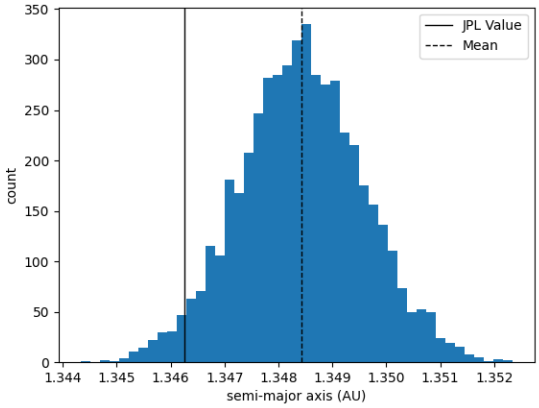

Figure 8. Monte Carlo: Semi-Major Axis

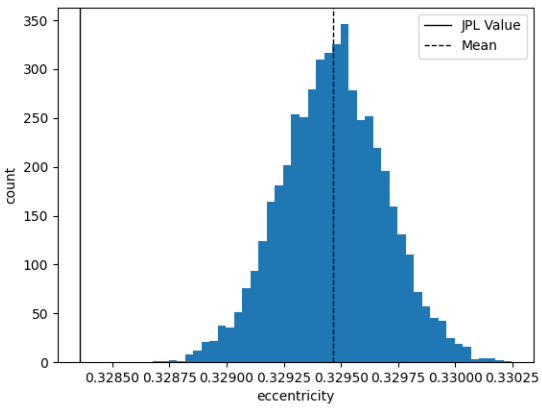

Figure 9. Monte Carlo: Eccentricity

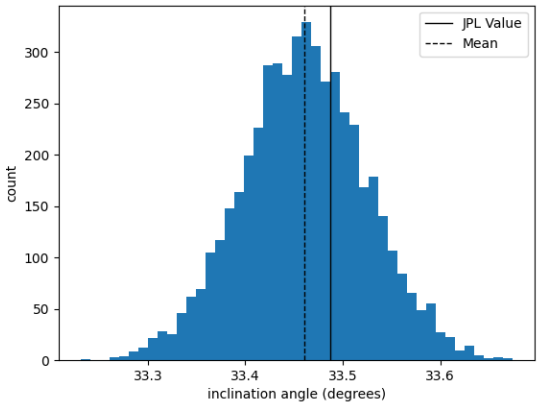

Figure 10. Monte Carlo: Inclination

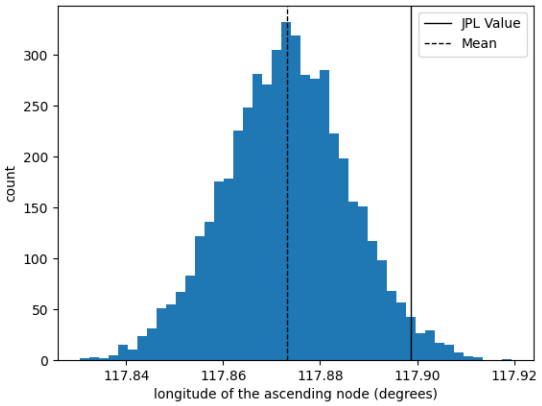

Figure 11. Monte Carlo: Ascending Node

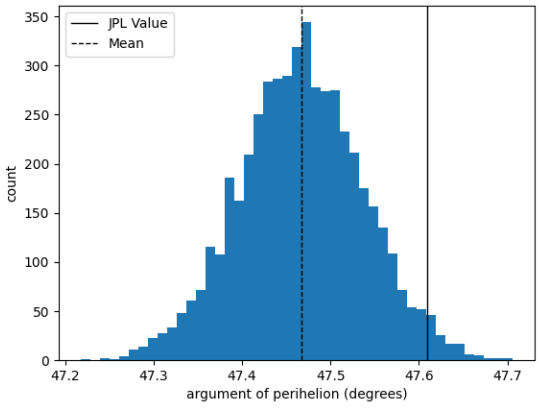

Figure 12. Monte Carlo: Perihelion

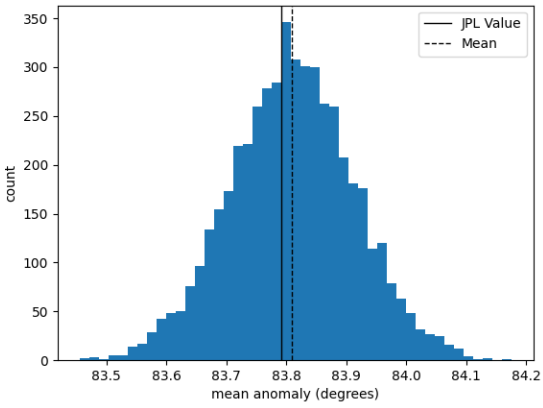

Figure 13. Monte Carlo: Mean Anomaly

Finally, using all the orbital elements calculated, a visualization of the orbit of 1994 PC1 was created (Figure 14).

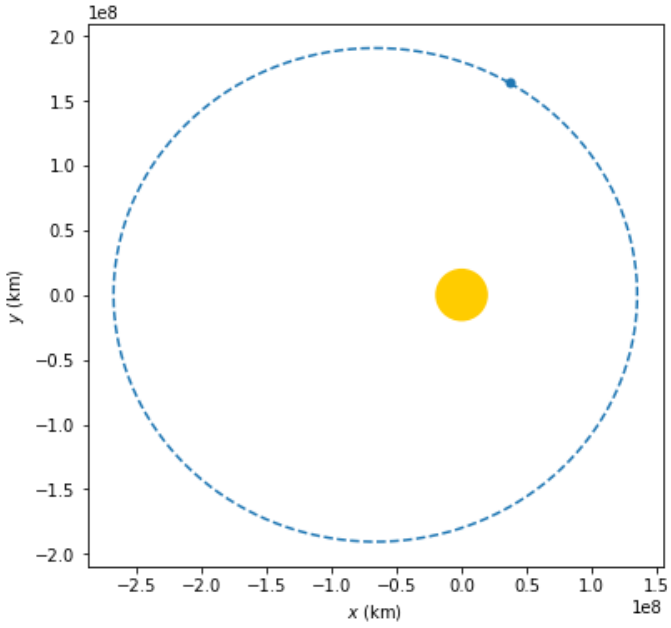

Figure 14. Visualization of 1994 PC1 using Calculated Orbit Elements

4. DISCUSSION

The calculated values for the orbital elements are relatively close to the values given by JPL horizons. From Table 4, all the calculated orbital elements were less than 0.5% off from the values reported by JPL. In addition, JPL's orbital elements were off the mean by less than 2 standard deviations in all calculated orbital elements besides eccentricity, which was off by almost 5 standard deviations. This suggests that there is a possibility that JPL's eccentricity for 1994 PC1 is not accurate, as the calculated values were successful in the self-consistency check.

The calculated RA and Dec for the third observation was relatively close to the observed value. The observed RA was within the error bars of the calculated RA, but the observed Dec was outside the error bars. The RAs and Decs were both within .25 arcseconds of each other.

There were several factors that may have impacted the results. During all observations, there was a crowded star field surrounding the asteroid. This made it difficult to place apertures during

astrometry that didn't contain other stars. This possibly affected the accuracy of the reported RA and Dec values. Also, since 1994 PC1 was low in the sky during each of the observations, light from the asteroid needed to pass through more airmass, resulting in more light diffraction and less clear imaging. By observing earlier in the night, the asteroid would have been higher in the sky, leading to clearer images and possibly lower errors in the observed RAs and Decs. In addition, the closed form formula for f and g could have been used instead of the fourth degree Taylor Series for increased accuracy, but this improvement is minimal. Lastly, differential correction and all four observations could have been used to get more accuracy on the orbital elements.

5. REFLECTION

This project was an incredible experience. It gave us the opportunity to combine what we have been learning and our observations into one coherent result, demonstrating the real-world applications of out learning. Our team particularly enjoyed observations, as it was an amazing and unique experience to operate complex telescopes ourselves to gather our data. All three team members evenly contributed during observations. While all team members contributed to the following aspects of the project, Matthew focused on compiling the orbital determination code, Gilbert did the majority of the photometry and astrometry of the images, and Ariella worked on compiling the Minor Planet Center report and the overall organization of the data. All team members equally contributed to the writing of this report.

Our team worked well together. We all had different strengths, and used them to our advantage. Each person was able to contribute well to a different aspect of the project, and this helped the team to succeed.

The one thing we wish we had done differently is to use our strengths to collaborate more closely while working together, rather than dividing the work. This is especially true for during the earlier parts of the program. However, for the most part, we are very happy with the way we completed the project. It was after all, the summer of a lifetime.

6. ACKNOWLEDGEMENTS

The following individuals have contributed to the success of this investigation by being instructors: Dr. Donovan Domingue, Dr. Michael Dubson, Mia Liang, Grace Edwards, Peter Lande, and Jessica Dong.

REFERENCES

[1]Diffraction Limited / SBIG. (n.d.). STF-8300. Diffractionlimited.com. https://diffractionlimited.com/wp-content/uploads/2018/06/AAS_STF.pdf

[2]Domingue, D. (Presenter). (2022, July 4). Orbital elements [Lecture].

[3]Garshnek, V., Morrison, D., Burkle, F. M. (2000). The mitigation, management, and survivability of asteroid/comet impact with earth. Space Policy, 16(3), 213-222. https://doi.org/10.1016/S0265-9646(00)00025-4

[4]Harris, A. W., Chodas, P. W. (2021). The population of near-earth asteroids revisited and updated. Icarus, 365. https://doi.org/10.1016/j.icarus.2021.114452

[5]Henden, A. A., Templeton, M., Terrell, D., Smith, T. C., Levine, S., Welch, D. (2016). VizieR Online Data Catalog: AAVSO Photometric All Sky Survey (APASS) DR9 [Abstract]. American Astronomical Society, (January).

[6]Irizarry, E. (2022, January). Photos and video of huge asteroid 1994 PC1. It passed Earth safely January 18. EarthSky. https://earthsky.org/space/asteroid-1994-pc1-closest-jan-18-2022/

[7]Jones, R. L., Slater, C. T., Moeyens, J., Allen, L., Axelrod, T., Cook, K., Ivezić, Ž., Jurić, M., Myers, J., Petry, C. E. (2018). The large synoptic survey telescope as a near-earth object discovery machine. Icarus, 303, 181-202. https://doi.org/10.1016/j.icarus.2017.11.033

[8]NASA. (2014, March 31). Asteroid fast facts. Nasa.gov. https://www.nasa.gov/mission_pages/asteroids/overview/fastfacts.html

[9]PlaneWave Instruments. (n.d.). CDK20 optical tube assembly (f/6.8). Planewave.com. https://planewave.com/product/cdk20-ota/

[10]University of Colorado Boulder. (n.d.). About Sommers-Bausch Observatory. Colorado.edu. https://www.colorado.edu/sbo/about-sommers-bausch-observatory

[11]Wall, M. (2014, June 18). Earth impact: Are comets a bigger danger than asteroids? Space.com. https://www.space.com/26264-asteroids-comets-earth-impact-risks.html